PROCEEDINGS OF SCIENCE

^{26}Al Gamma-ray Line Emission From Solar System Bodies

Tatsuki Fujiwara[a,*] **and Yoshiyuki Inoue**[a]

[a] *Department of Earth and Space Science, Graduate School of Science, Osaka University, Toyonaka, Osaka 560-0043, Japan*

E-mail: fujiwara@astro-osaka.jp, yinoue@astro-osaka.jp

In the Solar system, the radioisotope ^{26}Al exists on the surface of celestial bodies due to nuclear spallation by low-energy cosmic rays. Meteorites sampled on the Earth and lunar samples allow us to measure current ^{26}Al decay rate in laboratories. Based on these decay rates, we investigate the expected ^{26}Al gamma-ray line signals from solar system bodies, specifically asteroids in the main belt and the Moon. We find that the signals from the main belt are too weak to be detected by future planned MeV gamma-ray missions. However, due to its proximity and mass, next generation MeV gamma-ray mission such as the Compton Spectrometer and Imager (COSI) satellite will be able to detect ^{26}Al signals from the Moon. A future measurement of ^{26}Al will help us to understand lunar geology.

38th International Cosmic Ray Conference (ICRC2023)
26 July - 3 August, 2023
Nagoya, Japan

*Speaker

https://pos.sissa.it/

PoS(ICRC2023)680

1. Introduction

^{26}Al is one of the radioisotopes that exists outside Earth. It produces 1.8 MeV gamma-rays when it decays, with a half-life of 0.72 Myr. This ^{26}Al line is one of the target gamma-ray emission lines for MeV gamma-ray observations, such as those conducted with the Imaging Compton Telescope (COMPTEL) [1] and the future Compton Spectrometer and Imager (COSI) [2]. These missions focus on Galactic ^{26}Al to search for recent nucleosynthesis events caused by massive stars (e.g., [3]). However, in the Solar system, ^{26}Al also exists on the surface of airless celestial bodies, such as the Moon and asteroids, due to nuclear spallation processes driven by collisions of low-energy cosmic rays (CRs). Meteorites of asteroid origin sampled on the Earth, and lunar samples that were collected by Apollo program are known to contain ^{26}Al (e.g., [4, 5]). Although the number of samples is limited, they allow us to measure its current decay rate in laboratories (e.g., [6]). In this study, we report the expected ^{26}Al line signals from Solar system bodies based on these reported ^{26}Al decay rates. We specifically consider the Moon and main belt asteroids (MBAs) between the Mars and Jupiter (~ 2-3 au) as target celestial bodies.

2. Methods and Results

2.1 Experimental measurements of Aluminium-26 content in meteorites

Meteorites that originate from asteroids sampled on Earth and lunar samples collected by the Apollo program contain ^{26}Al. Figure 1 shows the ^{26}Al content (decay rate) of these measured samples ([7], [8] and references therein). Figures 1(a) and 1(b) show the ^{26}Al decay rate of lunar samples and those of meteorites originating from asteroids sampled in the Antarctic, respectively. It can be seen from the black solid lines in Figure 1 that lunar samples and antarctic meteorite samples approximately follow a log-normal distribution and normal distribution, respectively. The mean values from these fittings are $2.2 \times 10^{-3}\ \mathrm{s^{-1}g^{-1}}$ for lunar samples and $8.8 \times 10^{-4}\ \mathrm{s^{-1}g^{-1}}$ for antarctic meteorites.

In this study, we assume the ^{26}Al content for the entire lunar surface is $\epsilon_{☾} = 2.2 \times 10^{-3}\ \mathrm{s^{-1}g^{-1}}$, and that for all MBAs is $\epsilon_{\mathrm{MBA}} = 8.8 \times 10^{-4}\ \mathrm{s^{-1}g^{-1}}$. Moreover, we consider that each celestial body has a uniform ^{26}Al content across its surface. Therefore, by determining the interaction volume of CRs with the matter in celestial bodies, we can derive their total 1.8 MeV photon production rate. This is because ^{26}Al is produced through nuclear spallation by low-energy CRs.

2.2 Aluminium-26 gamma-ray flux from the Moon

We treat the Moon as a perfect sphere with a radius $R_{☾}$ of 1.737×10^8 cm [9] and with a uniform density distribution on its surface.

To derive the CR bombardment region of the Moon, we evaluated a CR penetration length Δr as a mean free path of CR protons through inelastic collisions with the matter of the lunar surface:

$$\Delta r = \frac{1}{\int_{10\,\mathrm{MeV}}^{200\,\mathrm{MeV}} I_\mathrm{p}(E)\mathrm{d}E} \int_{10\,\mathrm{MeV}}^{200\,\mathrm{MeV}} \mathrm{d}E \left(\sum_i n_i \sigma_{i\mathrm{p}}(E) \right)^{-1} I_\mathrm{p}(E), \tag{1}$$

where n_i is the number density of element i on the lunar surface, $\sigma_{i\mathrm{p}}(E)$ is the inelastic cross-section of element i for injected protons with kinetic energy E, and $I_\mathrm{p}(E)$ is CR proton intensity.

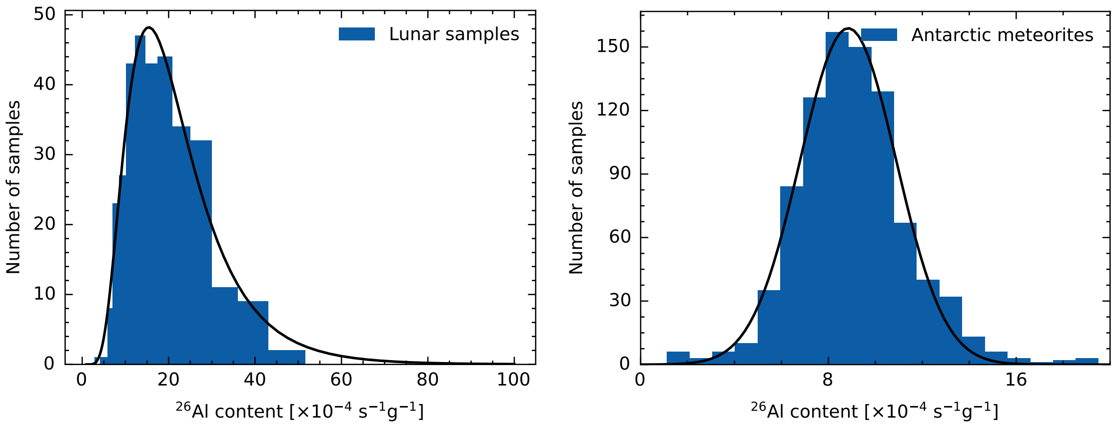

(a) (b)

Figure 1: ^{26}Al content (decay rate) for 1(a): lunar samples, and for 1(b): antarctic meteorites of asteroid origin, respectively. The units [$\mathrm{s}^{-1}\mathrm{g}^{-1}$] show ^{26}Al decay rate per unit sample mass. Solid lines of 1(a) and 1(b) show these fittings by a log-normal distribution and a normal distribution, respectively. These data are taken from [7], [8] and references therein.

To estimate the number density n_i of representative species (i = O, Na, Mg, Al, Si, Ca, Ti, Fe), we consider two possible lunar chemical compositions and mass densities, following [10] and [11]. These different n_i and $\rho_{\leftmoon}$ values do not have a substantial effect on our final results, i.e., the expected ^{26}Al photon flux from the Moon (cf., table I of [12].). We collected the corresponding cross-section data $\sigma_{ip}(E)$ using `TALYS` nuclear reaction code [13]. `TALYS` can calculate the cross-section up to injected particle energies of 200 MeV. We consider an energy range between 10 to 200 MeV in our calculation in order to capture the peak of the inelastic cross-sections. We construct a broken power-law model for the CR proton spectrum $I_\mathrm{p}(E)$, where the lower-energy component, below ~ 630 MeV[1], is obtained by fitting to the local interstellar CR proton spectrum (LIS) measured by *Voyager 1* [15]. The higher energy component is set by gauging against the spectrum obtained by *Fermi*-LAT observations of gamma-rays from the Moon [12], which follow a power-law of index -2.7. We then modify the spectrum to account for the solar modulation effect using the force field approximation [16], which yields a spectral index of ~0.84 below the break point. From Eq.(1) and lunar compositions of [10], we obtained a value of $\Delta r \simeq 33$ cm. Since $\Delta r \ll R_{\leftmoon}$, we can treat the ^{26}Al contained region as a spherical shell with a volume of $4\pi R_{\leftmoon}^2 \Delta r$.

The MeV photons produced by ^{26}Al can undergo interactions with matter in the lunar interior. From sub-MeV energies to a few MeV, gamma-ray interactions with matter are dominated by Compton scattering (e.g., [17]), which we consider as the main process governing photon-matter interactions in this work. Since we are interested only in 1.8 MeV photons, we can regard this process as 'self absorption' with an absorption coefficient α of $[\sigma_{\mathrm{KN}<1.8>} \sum_i Z_i n_i]$, where $\sigma_{\mathrm{KN}<1.8>}$ is the Klein-Nishina cross-section at 1.8 MeV (e.g., [17]) and Z_i is the atomic number of an element i; $\alpha \simeq 0.14\ \mathrm{cm}^{-1}$.

[1]Here, the break-point estimated by gauging against the spectrum model of [14].

We now derive ^{26}Al photon production rate of the Moon $L_{☾}$:

$$L_{☾} = 4\pi R_{☾}^2 \, \Delta r \, \rho_{☾} \, \epsilon_{☾} \, \frac{1 - \exp(-\alpha \Delta r)}{\alpha \Delta r}. \tag{2}$$

The factor of $[1 - \exp(-\alpha\Delta r)] / (\alpha\Delta r)$ comes from the slab approximation of self-absorption environment [18]. Therefore, we can determine the expected ^{26}Al photon flux from the Moon $F_{☾}$:

$$\begin{aligned} F_{☾} &= \frac{L_{☾}}{4\pi l_{\mathrm{EM}}^2} = \left(\frac{R_{☾}}{l_{\mathrm{EM}}}\right)^2 \Delta r \, \rho_{☾} \, \epsilon_{☾} \, \frac{1 - \exp(-\alpha\Delta r)}{\alpha\Delta r} \\ &\simeq 4.5 \times 10^{-6} \left(\frac{\Delta r}{33\ \mathrm{cm}}\right) \left(\frac{\epsilon_{☾}}{2.2 \times 10^{-3}\ \mathrm{s^{-1} g^{-1}}}\right) [\mathrm{ph/cm^2/s}], \end{aligned} \tag{3}$$

where $l_{\mathrm{EM}} = 3.844 \times 10^{10}$ cm, which is the distance (semi-major axis) between the Earth and Moon [9]. Note that the Moon should be treated as a point source in the MeV domain due to the angular resolution. The angular resolution of COSI at 1.8 MeV will be 1.5° FWHM [2], while the angular diameter of the Moon is about 0.5° [9]. According to [2], COSI will have a line sensitivity of 1.7×10^{-6} ph/cm^2/s at 1.8 MeV (assuming a 2-year survey). Thus, we expect that COSI will be able to detect the ^{26}Al gamma-ray signals from the Moon.

2.3 Aluminium-26 photon intensity from the main belt

For MBAs, the derived quantity should be intensity—not be flux— since COSI cannot distinguish each asteroid in the main belt due to its angular resolution. We first derive the total flux from the MBAs and the solid angle of the main belt measured from the Earth, then we derive the total intensity.

We treat each asteroid as a perfect sphere with a homogeneous density distribution in the same way as in Section 2.2. As parameters for MBAs, we only considered asteroid size (diameter) D, semi-major axis a, spectral type of asteroid j_{s}, and orbital inclination angle to the ecliptic i. If considering a stationary asteroid at a position A, located at a distance a from the Sun (at a position O), and tilted at an inclination i, then the angle $\theta_{\mathrm{OCA}} = \angle\mathrm{OCA}$ can be defined, where point C represents the location of COSI. θ_{OCA} changes as COSI orbits around Earth. The distance CA is thus a function of a and θ_{OCA}, or represented as $l_{\mathrm{CA}}(a, \theta_{\mathrm{OCA}})$, which is given as $l_{\mathrm{CA}}(a, \theta_{\mathrm{OCA}}) = \cos(\theta_{\mathrm{OCA}}) + \sqrt{\cos^2(\theta_{\mathrm{OCA}}) + a^2 - 1}$ in au. Both the maximum and the minimum θ_{OCA} are functions of a and i. Thus, the mean of l_{CA} over θ_{OCA} can also be expressed as a function with respect to a and i. Since it is enough for us to know the average value of l_{CA}, it is not necessary to consider θ_{OCA} as a variable, but as a function of a and i. We also assume that the main belt is symmetrically distributed around an axis perpendicular to the ecliptic plane centered on the Sun.

For an asteroid with parameters $(D, a, j_{\mathrm{s}}, i)$, we can obtain an expression for its ^{26}Al photon flux f_{A} in the same manner as Eq.(3):

$$f_{\mathrm{A}}(D, a, j_{\mathrm{s}}, i) = \frac{1}{4} D^2 \left\langle \frac{1}{l_{\mathrm{CA}}^2} \right\rangle \Delta r \, \rho_{j_{\mathrm{s}}} \, \epsilon_{\mathrm{MBA}} \, \frac{1 - \exp(-\alpha\Delta r)}{\alpha\Delta r}, \tag{4}$$

where $\langle l_{\mathrm{CA}}^{-2} \rangle$ is the average of l_{CA}^{-2} with respect to θ_{OCA} (this is the function of a and i). For the CR penetration length Δr, using chemical composition of CI chondrites [19], an asteroid average mass density of 2.0 g/cm^3 [20, 21], and the corresponding cross-section data from `TALYS`, we obtain $\Delta r \simeq 50$ cm. Due to insufficient data for the chemical composition of asteroids, we use CI chondrite abundances here, which is known to be the most primitive meteorite [19]. Here we set the CR proton intensity I_p in the main belt to be the same as I_p around the Moon (Section 2.2). The same applies to α as in Section 2.2; $\alpha \simeq 9.4 \times 10^{-2}$ cm^{-1}. The mass density ρ_{j_s} is obtained from [20] and references therein (see their Table 2).

To calculate the total ^{26}Al flux from the MBAs, we consider the main belt distribution of asteroid sizes D, semi-major axes a, spectral types j_s, and inclination angles i. We assume that the distribution function for the MBAs $\Pi\,(D,\ a,\ j_\mathrm{s},\ i)$ takes the following form:

$$\Pi\,(D,\ a,\ j_\mathrm{s},\ i) = C\, P_\mathrm{size}(D)\, P_\mathrm{sp}(a)\, P_\mathrm{type}(a;\ j_\mathrm{s})\, P_\mathrm{inc}(i), \tag{5}$$

where $P_\mathrm{size}(D)$ is the differential size distribution, $P_\mathrm{sp}(a)$ is the spatial distribution, $P_\mathrm{type}(a;\ j_\mathrm{s})$ is the fractional distribution for spectral types, $P_\mathrm{inc}(i)$ is the fractional distribution for inclination angle, and C is the normalization constant. For these distributions, we collected data from observational literature and databases, as shown in Figure 2. We determined the constant C by normalizing Π by the total mass of the main belt:

$$M_\mathrm{tot} - \sum_{k=1,2,4,10} M_{(k)} = C \int \mathrm{d}D\mathrm{d}a \sum_{j_\mathrm{s}} P_\mathrm{size}(D)\, P_\mathrm{sp}(a)\, P_\mathrm{type}(a;\ j_\mathrm{s})\, \frac{4}{3}\pi \left(\frac{D}{2}\right)^3 \rho_{j_\mathrm{s}}, \tag{6}$$

where $M_\mathrm{tot} = 2.394 \times 10^{24}$ g: the total mass of the main belt [22] and $M_{(k)}$ is the mass of the four largest MBAs: (1) Ceres, (2) Pallas, (4) Vesta, and (10) Hygiea based on recent observations [23] (see their Table 1). As inferred from Eq.(6), we eliminate the four largest asteroids from the distribution function and calculate their gamma-ray flux individually [following 23][2]. This adjustment is due to discrepancies between $D_{(k)}$ used in P_size $(D > 332\,\mathrm{km})$ in [25] (see their Table 1) and $D_{(k)}$ in [23]. Typically, information about sub-km sized asteroids is limited, indicating observations are biased. Since larger asteroids have a greater impact on M_tot, we use Π normalized by the mass of observed MBAs rather than by the number that have been detected.

We derive the total flux from the MBAs F_MBAs as follows:

$$F_\mathrm{MBAs} = \int \mathrm{d}D\mathrm{d}a \sum_{j_\mathrm{s},\,i} \Pi\,(D,\ a,\ j_\mathrm{s},\ i)\ f_\mathrm{A}(D,\ a,\ j_\mathrm{s},\ i) + \sum_{k=1,2,4,10} f_\mathrm{A}(D_{(k)},\ a_{(k)},\ i_{(k)}). \tag{7}$$

We also obtain the maximum solid angle of the main belt Ω_max as $\Omega_\mathrm{max} \simeq 7.7$ sr, considering the maximum inclination of 35.2° (see, Figure 2(d)). We obtain a value for Ω_max by taking the average of the solid angle measured with the minimum and maximum distances, l_CA. We used $P_\mathrm{size}(D)$, $P_\mathrm{sp}(a)$, $P_\mathrm{type}(a;\ j_\mathrm{s})$ in taking the average.

Now we can determine the expected ^{26}Al photon intensity from the main belt I_MBAs:

$$I_\mathrm{MBAs} = \frac{F_\mathrm{MBAs}}{\Omega_\mathrm{max}} \sim 2 \times 10^{-13} \left(\frac{\Delta r}{50\ \mathrm{cm}}\right) \left(\frac{\epsilon_\mathrm{MBA}}{8.8 \times 10^{-4}\ \mathrm{s^{-1} g^{-1}}}\right) \left(\frac{\Omega_\mathrm{max}}{7.7\ \mathrm{sr}}\right)^{-1} [\mathrm{ph/cm^2/s/sr}]. \tag{8}$$

Therefore, we expect that ^{26}Al gamma-ray signals from the main belt would be too weak to be detectable, even for up-coming MeV gamma-ray missions.

[2]Since the semi-major axis $a_{(k)}$ and the inclination $i_{(k)}$ are not given, we use data from [24].

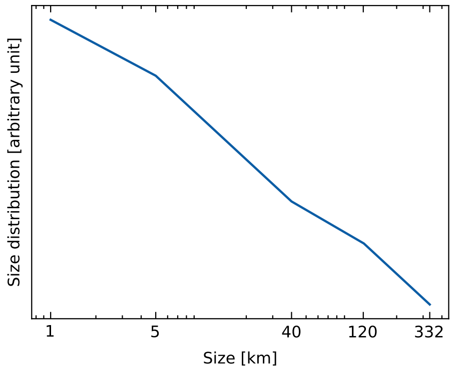

(a)

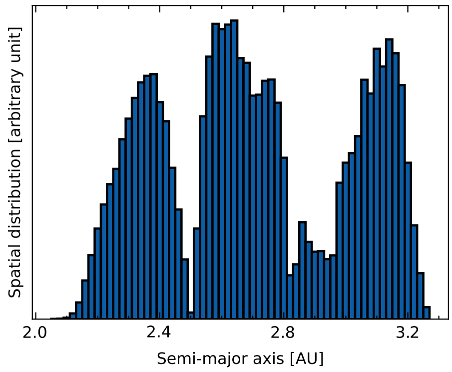

(b)

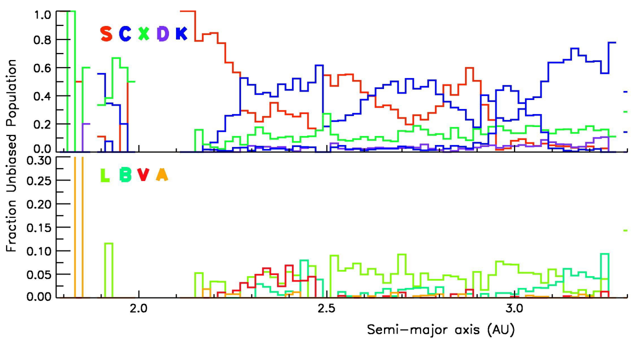

(c)

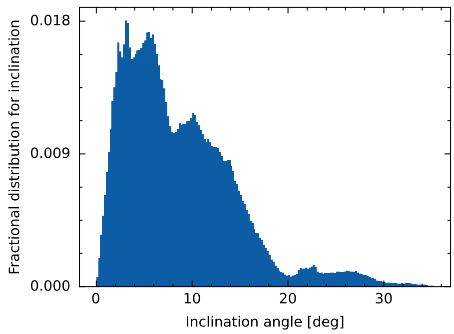

(d)

Figure 2: The distribution function of MBAs. As we adopt normalized distributions in our calculations, the y axes are shown in arbitrary units.
2(a): $P_{\rm size}(D)$ is defined as a broken power law function in $1 \leq D \leq 332$, with break points $D = 5,\ 40,\ 120$ as shown. 332 km is the size of the fifth largest asteroid: (704) Interamnia [23]. In increasing order of D, the spectral index s changes as $s = 2.3,\ 4.0,\ 2.5,\ 4.0$, where the first two indices are obtained from Sloan Digital Sky Survey observations [26], and the last two are determined by fitting the cumulative size distribution in [25].
2(b): $P_{\rm sp}(a)$ is defined the same range and the same bin as 2(c) below, collected with Small-Body Database Query [27].
2(c): $P_{\rm type}(a;\ j_{\rm s})$ is the fractional distribution with respect to a in $2.05 \leq a \leq 3.27$ with each bin of 0.02. The data and this plot are taken from [20]. The legends show spectral types of asteroids based on their classification. In [20], they only considered asteroids larger than 5 km for the bias-corrected population. However, in this study, we consider that $P_{\rm type}$ is applicable for sizes down to 1 km.
2(d): $P_{\rm inc}(i)$ is defined in $0 \leq i \leq 35.2$ with each bin of 0.2 [24].

3. Discussion and Conclusion

We find that the expected ^{26}Al photon flux from the Moon is $\sim 4.5 \times 10^{-6}$ ph/cm^2/s and the intensity from the main belt is $\sim 2 \times 10^{-13}$ ph/cm^2/s/sr, based on ^{26}Al decay rate of the extraterrestrial samples. These values are below COMPTEL sensitivity of $\sim 10^{-5}$ ph/cm^2/s at 1.8 MeV [2], which is consistent with previous non-detections. From the lunar result, we also find that the next generation MeV gamma-ray missions such as COSI will be able to detect the ^{26}Al signals from the Moon over a 2-year operation time. According to the gamma-ray albedo (continuum spectrum) of the Moon from sub-MeV to a few GeV energy range derived in [11] (see also [21]), the ^{26}Al line emission is about 20% of the continuum at 1.8 MeV.

In conclusion, although our current knowledge of lunar ^{26}Al is mainly limited to the Apollo samples, future MeV gamma-ray measurements will help us understand its abundance across the lunar surface.

References

[1] V. Schoenfelder, H. Aarts et al., *Instrument Description and Performance of the Imaging Gamma-Ray Telescope COMPTEL aboard the Compton Gamma-Ray Observatory*, ApJS **86** (1993) 657.

[2] J. Tomsick, A. Zoglauer et al., *The Compton Spectrometer and Imager*, in *Bulletin of the American Astronomical Society*, vol. 51, p. 98, Sept., 2019, DOI [1908.04334].

[3] R. Diehl and F.X. Timmes, *Gamma-Ray Line Emission from Radioactive Isotopes in Stars and Galaxies*, PASP **110** (1998) 637.

[4] K. Fuse and E. Anders, *Aluminum-26 in meteorites - VI. Achondrites*, Geochim. Cosmochim. Acta **33** (1969) 653.

[5] Lunar Sample Preliminary Examination Team 1, *Preliminary Examination of Lunar Samples from Apollo 11*, *Science* **165** (1969) 1211.

[6] E. Anders, *The record in the meteorites—II on the presence of aluminium-26 in meteorites and tektites*, Geochim. Cosmochim. Acta **19** (1960) 53.

[7] C. Meyer, *Lunar Sample Compedium*, `https://curator.jsc.nasa.gov/lunar/lsc/index.cfm`, 2012 [Accessed: 2023-06-29].

[8] J. Wacker, J. Reeves et al., *Antarctic Meteorite Collection*, `https://curator.jsc.nasa.gov/antmet/us_clctn.cfm`, 2022 [Accessed: 2023-07-04].

[9] D.R. Williams, *Moon Fact Sheet*, `https://nssdc.gsfc.nasa.gov/planetary/factsheet/moonfact.html`, 2021.

[10] A.L. Turkevich, *Average Chemical Composition of the Lunar Surface*, *Moon* **8** (1973) 365.

[11] I.V. Moskalenko and T.A. Porter, *The Gamma-Ray Albedo of the Moon*, ApJ **670** (2007) 1467 [0708.2742].

[12] M. Ackermann, M. Ajello et al., *Measurement of the high-energy gamma-ray emission from the Moon with the Fermi Large Area Telescope*, Phys. Rev. D **93** (2016) 082001 [1604.03349].

[13] A.J. Koning, S. Hilaire et al., *Talys-1.0*, in *International Conference on Nuclear Data for Science and Technology*, pp. 211–214, EDP Sciences, 2007.

[14] E. Orlando, *Imprints of cosmic rays in multifrequency observations of the interstellar emission*, MNRAS **475** (2018) 2724 [1712.07127].

[15] A.C. Cummings, E.C. Stone et al., *Galactic Cosmic Rays in the Local Interstellar Medium: Voyager 1 Observations and Model Results*, ApJ **831** (2016) 18.

[16] L.J. Gleeson and W.I. Axford, *Solar Modulation of Galactic Cosmic Rays*, ApJ **154** (1968) 1011.

[17] M.S. Longair, *High Energy Astrophysics*, Cambridge University Press (2011).

[18] C.D. Dermer and G. Menon, *High Energy Radiation from Black Holes. Gamma Rays, Cosmic Rays, and Neutrinos*, Princeton University Press (2010).

[19] M. Asplund, A.M. Amarsi et al., *The chemical make-up of the Sun: A 2020 vision*, A&A **653** (2021) A141 [2105.01661].

[20] F.E. DeMeo and B. Carry, *The taxonomic distribution of asteroids from multi-filter all-sky photometric surveys*, Icarus **226** (2013) 723 [1307.2424].

[21] I.V. Moskalenko, T.A. Porter et al., *A Celestial Gamma-Ray Foreground Due to the Albedo of Small Solar System Bodies and a Remote Probe of the Interstellar Cosmic-Ray Spectrum*, ApJ **681** (2008) 1708 [0712.2015].

[22] E.V. Pitjeva and N.P. Pitjev, *Masses of the Main Asteroid Belt and the Kuiper Belt from the Motions of Planets and Spacecraft*, *Astronomy Letters* **44** (2018) 554 [1811.05191].

[23] P. Vernazza, M. Ferrais et al., *VLT/SPHERE imaging survey of the largest main-belt asteroids: Final results and synthesis*, A&A **654** (2021) A56.

[24] IAU Minor Planet Center, *MPC Database Search*, https://minorplanetcenter.net/db_search, 2023 [Accessed: 2023-04-06].

[25] W.F. Bottke, D.D. Durda et al., *The fossilized size distribution of the main asteroid belt*, Icarus **175** (2005) 111.

[26] Ž. Ivezić, S. Tabachnik et al., *Solar System Objects Observed in the Sloan Digital Sky Survey Commissioning Data*, AJ **122** (2001) 2749 [astro-ph/0105511].

[27] Jet Propulsion Laboratory, *Small-Body Database Query*, https://ssd.jpl.nasa.gov/tools/sbdb_query.html, 2023 [Accessed: 2023-05-23].